Inferring the Variability of Dielectric Constant on the Moon from Mini-RF S-Band Observations

Shukla, Shashwat; Patterson, Gerald Wesley; Maiti, Abhisek; Kumar, Shashi; Dutton, Nicholas

Important note
To cite this publication, please use the final published version (if applicable).
Please check the document version above.

Inferring the Variability of Dielectric Constant on the Moon from Mini-RF S-Band Observations

Shashwat Shukla [1],[*] , Gerald Wesley Patterson [2], Abhisek Maiti [3], Shashi Kumar [4] and Nicholas Dutton [2]

1   Department of Geoscience and Remote Sensing, Delft University of Technology,
    2628 CN Delft, The Netherlands
2   Space Exploration Sector, Johns Hopkins University Applied Physics Laboratory, Laurel, MD 20723, USA;
    wes.patterson@jhuapl.edu (G.W.P.); nicholas.dutton@jhuapl.edu (N.D.)
3   Faculty of Geo-Information Science and Earth Observation, University of Twente,
    7522 NH Enschede, The Netherlands; a.maiti@utwente.nl
4   Indian Institute of Remote Sensing, Indian Space Research Organization (ISRO), Dehradun 248001, India;
    shashi@iirs.gov.in or shashikumar@iirsddn.ac.in
*   Correspondence: s.shukla@tudelft.nl

Abstract: The physical properties of lunar regolith are crucial for exploration planning, hazard assessment, and characterizing scientific targets at global and polar scales. The dielectric constant, a key property, offers insights into lunar material distribution within the regolith and serves as a proxy for identifying volatile-rich regoliths. Miniature radio frequency (Mini-RF) on the Lunar Reconnaissance Orbiter (LRO) provides a potential tool for mapping the lunar regolith's physical nature and assessing the lunar volatile repository. This study presents global and polar S-band Mini-RF dielectric signatures of the Moon, obtained through a novel deep learning inversion model applied to Mini-RF mosaics. We achieved good agreement between training and testing of the model, yielding a coefficient of determination (R^2 value) of 0.97 and a mean squared error of 0.27 for the dielectric constant. Significant variability in the dielectric constant is observed globally, with high-Ti mare basalts exhibiting lower values than low-Ti highland materials. However, discernibility between the South Pole–Aitken (SPA) basin and highlands is not evident. Despite similar dielectric constants on average, notable spatial variations exist within the south and north polar regions, influenced by crater ejecta, permanently shadowed regions, and crater floors. These dielectric differences are attributed to extensive mantling of lunar materials, impact cratering processes, and ilmenite content. Using the east- and west-looking polar mosaics, we estimated an uncertainty (standard deviation) of 1.01 in the real part and 0.03 in the imaginary part of the dielectric constant due to look direction. Additionally, modeling highlights radar backscatter sensitivity to incidence angle and dielectric constant at the Mini-RF wavelength. The dielectric constant maps provide a new and unique perspective of lunar terrains that could play an important role in characterizing lunar resources in future targeted human and robotic exploration of the Moon.

Keywords: Moon; physical properties; dielectric constant; Mini-RF; deep learning; inversion model

1. Introduction

Our current knowledge of the lunar crust suggests that lateral variations in composition are crucial for identifying the structure and distribution of materials on the Moon [1,2]. Based on the composition of surface materials, the lunar crust can be categorized into distinct geological regions [3]. However, these materials also possess unique physical properties that have a notable impact on the spatial differences in near-surface composition. One such property is the dielectric constant, which measures how easily a material can be polarized in response to an electric field. The dielectric constant is a complex parameter: (a) the real part quantifies the electric polarizability of a dielectric medium, whereas (b) the imaginary part quantifies a dielectric material's inherent dissipation of electromagnetic

(EM) energy. A high dielectric constant indicates that the material can store a significant amount of electrical energy, while a low dielectric constant implies that the material is less able to store electrical energy.

Studying the dielectric properties of the lunar regolith is important for several reasons: (a) Material distribution: The dielectric constant reveals important clues about the distribution of materials within the regolith. Different materials have distinct dielectric properties, allowing us to identify and map their presence across the lunar surface. This knowledge is useful for gaining a better understanding of the Moon's composition and its geological history. (b) Unraveling surface features: Analyzing the dielectric constant helps us understand the origin and evolution of lunar surface features. Variations in dielectric properties indicate changes in material composition, porosity, or moisture content, providing insights into the processes that have shaped the Moon's surface over time. (c) Volatile detection: As the dielectric constant, to a first order, is used as a density proxy, it can also provide important information about the volatiles trapped in the lunar regolith. Volatiles are essential resources for future lunar missions, offering potential sources of water for life support and fuel production. By quantifying dielectric properties, we can improve our ability to locate and precisely characterize these valuable resources.

In the 1970s, the Apollo and Luna missions collectively retrieved 387.1 kg and 0.3211 kg of lunar samples, respectively. Subsequent laboratory analyses, conducted in studies such as [4–7], encompassed measurements of density, complex permittivity, and chemical composition. The outcomes of these investigations revealed significant correlations. Specifically, the real component of the dielectric constant in lunar samples demonstrated dependence on bulk density, while the imaginary component was found to be associated with both bulk density and the abundance of ilmenite ($FeO + TiO_2$). Moreover, China's Chang'E-5 mission achieved a successful retrieval of 1.731 kg of lunar samples from the Oceanus Procellarum, as documented in studies by Qian et al. [8] and Li et al. [9]. While in situ sampling from the lunar surface offers the most direct insights into the regolith, it is important to note that these samples are presently gathered exclusively at 10 landing sites located in the central part of the Moon's nearside. Consequently, the information derived from these samples only provides a comprehensive understanding of the lunar regolith within the specific regions where sampling has occurred, as discussed in [10].

Remotely sensed radar data provides the potential to characterize the dielectric properties of the near surface and subsurface of the Moon's regolith on a global scale. This information is not only valuable for scientific purposes but also essential for supporting both human and robotic exploration endeavors. Earth-based radar studies have been used to investigate the physical nature of the lunar near surface for resource characterization, landing site hazards, lunar geologic history, and evaluation of physical properties (e.g., [11,12]). However, these data have limitations in accessing the lunar farside and in the geometries available for observing the lunar nearside. In this context, the Miniature Radio Frequency (Mini-RF) instrument on the NASA Lunar Reconnaissance Orbiter (LRO) offers global coverage of the lunar surface [13,14].

Measuring the dielectric constant of the lunar surface from remotely sensed radar data is not a straightforward process. Radar backscatter is sensitive to physical properties such as roughness, dielectric constant, regolith thickness, $FeO + TiO_2$ content, and buried rock abundance [15]. Moreover, radar frequency and incidence angle additionally impact the backscatter. Radiative transfer (RT) equations can be used to express the magnitude of radar backscatter as a function of physical properties and radar parameters, which can form the basis of a forward model [15]. While a forward model can establish a highly complex and nonlinear relationship between radar signal and surface properties, we additionally require an inversion approach along with forward modeling to quantify the dielectric constant from radar observations.

Currently, only a few studies have attempted to estimate the dielectric constant of lunar regolith through the inversion of radar data. Campbell et al. [16,17] conducted Earth-based radar observations to investigate the scattering properties of planetary surfaces. They de-

veloped an inversion model for the dielectric constant based on the co-polarization ratio of radar echoes. Their model assumes negligible cross-polarization components and that the radar backscatter from the subsurface is significantly stronger than that from the surface. As a result, this model is only applicable to flat lunar surface regions and often overestimates the dielectric constant [18]. On the other hand, Kumar et al. [19] developed a dielectric constant inversion technique based on measured LH and LV returns of Mini-RF. Here, a ratio of Fresnel reflection coefficient is derived using a three-component decomposition method, which is then numerically solved on a pixel-per-pixel basis to estimate the real part of the dielectric constant. A limitation of this approach is the numerical solver itself, which does not always converge to a numeric value. Specifically, the decomposition method used to separate different scattering processes from the radar data can be problematic. The separation is not always reliable, as it depends heavily on the accuracy of the model assumptions and the numerical solver. This can lead to results that are not directly correlated with the physical properties of interest, such as roughness or the dielectric constant, due to the inherent difficulties in quantifying these processes accurately [20].

Given the complex forward relationship of radar signals with physical properties, machine learning, especially artificial neural network (ANN), has demonstrated its utility as an emerging inversion approach in Earth-based retrieval studies [21]. Shukla [22] and Shukla et al. [23] employed the Integral Equation Model (IEM), which only includes surface scattering, as a forward model and multi-layer perceptron (MLP) ANN for inversion and applied it to lunar regolith. Another study utilized the IEM modeling technique in two-dimensional and three-dimensional simulations using the Chandrayaan-2 L-band DFSAR data for permanently shadowed regions (PSRs) with ANN as the inversion [24]. The penetration depth of L- and S-band suggests that the scattering contribution may not be likely from the top surface alone, thereby making the IEM less usable for the inversion approach. Furthermore, Gao et al. [25] applied the extended Bragg (X-Bragg) model to Mini-RF data and inverted the dielectric constant using a minimization approach. The proposed model, however, is limited to regolith fines in lunar PSRs and mid-latitude regions. None of the studies have fully integrated the Mini-RF data for global and polar perspectives of the dielectric constant.

We present a new inversion model for dielectric constant that uses spatially semi-controlled global and controlled polar Mini-RF S-band mosaics [2]. Here, we develop a two-layer lunar regolith model with five basic processes through direct scattering from the top surface and bedrock, diffuse scattering from buried inclusions, and scattering from the interaction between bedrock and buried inclusions. We parameterize the IEM for rough surface and derive the scattering contribution from a low dielectric layer of Rayleigh spheres with irregular regolith-bedrock boundaries. As part of the inversion, we develop a novel deep learning-based model to retrieve dielectric constant values. The robustness and reliability of the inversion are evaluated by comparing the retrieved dielectric constant with lunar sample drive core measurements [10]. Our approach addresses the limitations of previous models, which either involved surface scattering in the forward model or could only be used to invert the local dielectric constant for regolith fines and smooth mid-latitude regions.

2. Data and Methods

Mini-RF is a side-looking synthetic aperture radar (SAR) instrument that transmits circular polarization and receives coherently on orthogonal linear polarizations (H and V) at 12.6 cm (S-band) or 4.2 cm (X/C-band) wavelengths [26]. The data is acquired in either 'baseline' mode with 150 m spatial resolution or in 'zoom' mode with 30 m spatial resolution. In our work, we focus on S-band zoom data products, which are sensitive to

scatterers in the size range of >~0.1–1.26 m and penetrate to similar vertical depths [26]. Mini-RF data can be represented by the Stokes parameters S_1, S_2, S_3, S_4 [27]:

$$
\begin{aligned}
S_1 &= <|E_H|^2 + |E_V|^2> \\
S_2 &= <|E_H|^2 - |E_V|^2> \\
S_3 &= 2Re < E_H E_V^* > \\
S_4 &= -2Im < E_H E_V^* >
\end{aligned}
\tag{1}
$$

Here, *E* is the complex voltage in the subscripted polarization. Model inputs for the horizontal (E_H) and vertical (E_V) components are derived from Mini-RF Stokes parameter-controlled polar [28] and semi-controlled global [2] products. For this work, the global and polar products were down-sampled to spatial resolutions of 64 pixels/degree and 512 pixels/degree respectively. A lower resolution was used for the global product because it was semi-controlled, and a higher resolution for the polar products because they were fully controlled. The polar products included separate east-looking and west-looking data. These data were defined as consisting of individual Mini-RF data strips that had azimuthal look directions between 0°–180° and 180°–360°, respectively. Both datasets were included in the analysis to reduce potential look direction bias in the inverted results for the polar products. The proposed methodology is illustrated in Figure 1.
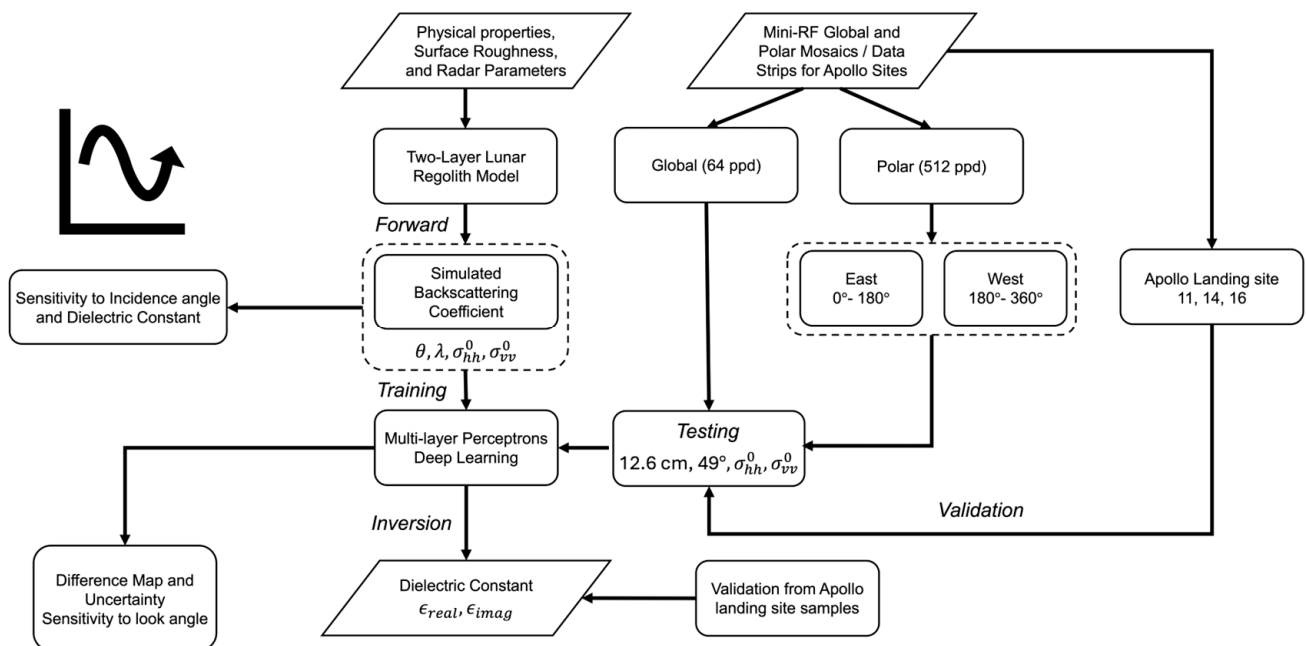

Figure 1. Schematic overview of the proposed framework in the research.

2.1. Impact of Physical Properties on Radar Backscatter: A Radiative Transfer Modeling Approach

Radiative transfer modeling is an effective approach to understanding the interaction between electromagnetic waves and the surface in the microwave region, thereby gaining insights into surface characteristics. Backscattering models provide a foundation for evaluating the electromagnetic (EM) response and the factors that influence it. Simulating the EM response of the Moon is a complex task that requires a comprehensive understanding of the EM properties of materials at a desired frequency range. While lunar samples have been extensively tested at frequencies below 1 GHz [10], challenges arise when dealing with frequencies > 1 GHz. This poses a time-consuming endeavor that demands significant effort. To address this, we attempted to replicate the EM response using a widely-used model commonly employed in soil studies [21].

For our analysis, we employ a two-layer lunar regolith model that considers the regolith to be a homogeneous fine-grained layer with buried inclusions between the top surface and bottom subsurface of well-defined roughness and dielectric constant, as shown in Figure 2. We represent five basic processes: (a) rough surface scattering from the top regolith, (b) volume scattering from buried inclusions, (c) subsurface scattering from bedrock, (d) subsurface-volume scattering from the interaction of the radar signal with bedrock first followed by buried inclusions, and (e) volume-subsurface scattering from the radar interaction with buried inclusions first followed by the bedrock.
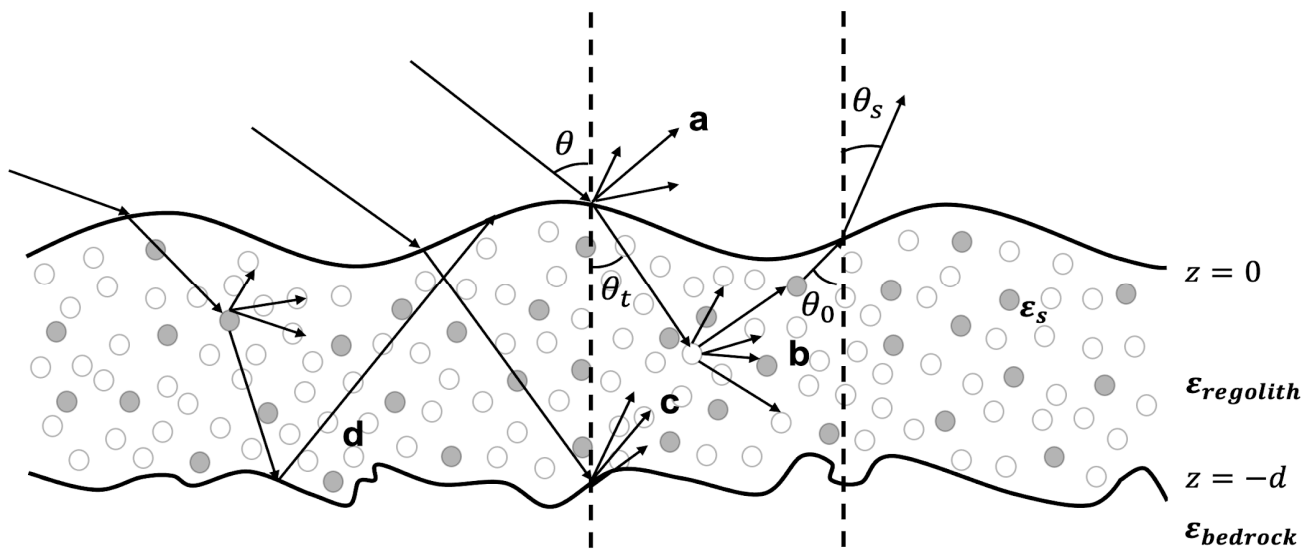

Figure 2. Scattering geometry of the lunar surface, consisting of regolith, embedded rocks, and underlying bedrock. Regolith grains are represented by a circular shape, whereas the buried inclusions (rocks) are denoted by shaded circles. These are randomly distributed across the regolith layer of thickness d. **a** is scattering from the top rough surface, **b** is volume scattering due to scatterers within the layer, **c** is subsurface scattering from the bedrock, and **d** represents the scattering due to surface-volume interaction. ε_s is the dielectric constant of buried inclusions, whereas $\varepsilon_{regolith}$ and $\varepsilon_{bedrock}$ are for the regolith layer and subsurface, respectively.

To model these five scattering processes, we parameterize the Integral Equation Model (IEM) for the rough surface and derive the scattering contribution from a low dielectric layer of Rayleigh spheres with irregular regolith-bedrock boundaries [29,30]. The Rayleigh parameters are extracted for estimating the absorption, scattering and transmission losses of the radar signal when interacting with the regolith at different depths. In this regard, the total radar backscatter from our two-layer lunar regolith model can be expressed as

$$\sigma^0_{total} = \sigma^0_{surf} + \sigma^0_{subsurf} + \sigma^0_{vol} + \sigma^0_{subsurf-vol} + \sigma^0_{vol-subsurf} \tag{2}$$

The rough surface scattering component from the top regolith is given by

$$\sigma^0_{surf} = \frac{k^2}{4\pi} e^{-2k^2\theta \, \sigma_1^2} \sum_{n=1}^{\infty} \left| I^n_{pp} \right|^2 \frac{w^{(n)}(2k\sin\theta, \, 0)}{n!} \tag{3}$$

where

$$I^n_{pp} = (2k\sigma_1 \cos\theta \,)^n f_{pp} e^{-k^2\theta \, \sigma_1^2} + (k\sigma_1 \cos\theta \,)^n F_{pp}, \; p = h, \, v \tag{4}$$

Here, k is a wavenumber and hence, dependent on the incident radar wavelength, σ_1 is the vertical component of roughness, represented by root mean squared (RMS) height, θ is the incidence angle of the sensor, f_{pp} is the Kirchhoff field coefficient, and F_{pp} represents the complementary field coefficient for either HH or VV polarization channels [30]. The

horizontal component of roughness or autocorrelation length is expressed in the form of an exponential surface correlation function, i.e., by $w^{(n)}(2k\sin\theta, \ 0)$. The exponential function is found to be well-suited for representing the natural surface conditions on both the Earth's surface and other planetary settings [15].

The second term is associated with the subsurface bedrock, where the radar signal is scattered from its direct incidence on the bedrock [15]. The radar signal, in such a scenario, is attenuated twice while passing from the top surface layer to the bottom and vice versa.

$$\sigma^0_{subsurf} = \mu_s T(\theta_s, \ \theta_0) e^{-\frac{\kappa_e d}{\mu_0}} \sigma_{surf}(\theta_t) e^{-\frac{\kappa_e d}{\mu_t}} \frac{T(\theta_t, \ \theta)}{\mu_t} \tag{5}$$

Here, the depth of the regolith layer is denoted by d, $\mu_s = cos \ \theta_s$, $\mu_t = coscos \ \theta_t$, and $\mu_0 = coscos \ \theta_0$, where θ_s is the scattering angle, θ_t is the transmission angle, and θ_0 is the incidence angle, respectively (as shown in Figure 2). The extinction coefficient is represented by κ_e and, hence, the optical depth is $\kappa_e d$. The power Fresnel transmission coefficient is denoted by $T(\theta_i, \ \theta_j)$, where i and j decide the respective angle of the radar signal as it travels in the regolith medium [29].

The third term is the volume scattering component from the buried inclusions, which may be either rocks or water ice.

$$\sigma^0_{vol} = \mu_s T(\theta_s, \ \theta_0) a \left(1 - e^{-\frac{\kappa_e d(\mu_0 + \mu_t)}{\mu_0 \mu_t}}\right) \frac{P(\mu_0, -\mu_t)}{\mu_0 + \mu_t} \mu_t T(\theta_t, \ \theta) \tag{6}$$

Here, the term $P(\mu_0, -\mu_t)$ is the Rayleigh phase function for horizontal and vertical polarizations, and a is the radar albedo, represented by the ratio of volume scattering coefficient κ_s and extinction coefficient κ_e.

The subsurface-volume and volume-subsurface terms are derived by considering the reciprocity condition, which necessarily makes both terms the same. In this scattering regime, the bedrock exhibits a significant coherent reflectivity, given by $R(\theta_0)e^{-k_l^2 \sigma_2^2 (\mu_0 + \mu_t)^2}$ [29]. Here, k_l is the radar wavenumber in the layer and σ_2 is the RMS height of bedrock.

$$\sigma^0_{subsurf-vol} = a\mu_s T^2(\theta_t, \ \theta) R(\theta_t) \frac{\kappa_e d}{\mu_t} e^{-2\frac{\kappa_e d}{\mu_t} - 4k_l^2 \sigma_2^2 \mu_t^2} [P(-\mu_t, -\mu_t) + P(\mu_t, \ \mu_t)] \tag{7}$$

The Rayleigh phase function, $P(-\mu_0, -\mu_t)$ is equal to $P(\mu_0, \ \mu_t)$. Since the above term is equal to $\sigma^0_{vol-subsurf}$, we sum this term two times with the other scattering components in the total backscatter equation. For a detailed derivation of individual scattering contributions, we refer to Fung and Chen [29]. Note that our model does not consider coherent backscatter opposition effects and multiple scattering events among the rocks.

2.1.1. Parameterization of Radiative Transfer Model

In our simulation, the autocorrelation length is assumed to be the same as the wavelength of incident radar waves (i.e., 12.6 cm) and is used with an exponential surface correlation function [15]. This assumption is due to the lack of surface roughness information comparable to the Mini-RF wavelength [15]. The variation in roughness is defined by the range of RMS height between 0 cm (very smooth) and 5 cm (very rough). Based on the Apollo and Luna samples, we have taken the FeO+TiO$_2$ wt% from 0 to 30 with a step of 0.5 [15]. Bulk density is assumed to be between 0.75 and 3.32 g/cm^3 [10]. One important parameter representing the quantitative presence of buried inclusions in the regolith is the volume fraction. We describe the limits of volume fraction between 0 and 0.1 with a step of 0.001. This parameter is then used in Lichtenecker's mixing rule to compute the effective dielectric constant of regolith with buried inclusions, such as silicate rocks [15]. We model the buried inclusion as a Rayleigh spherical scatterer with a radius varying from 0.5 cm to 5 cm [15]. Most of the scatterers are non-spherical. However, when they are randomly oriented and distributed within a layer, they can be approximated as a collection

of spherical scatterers [29]. Regolith thickness varies from 4 m to 15 m in the model. The incidence angle is further ranged between 0° and 80°, thereby capturing all the incidence angles of current state-of-the-art orbital S-band radar systems in lunar orbit [15]. In Table 1, the range of all the above parameters is considered either from the Apollo science data or from literature-based surveys [10,15,22]. Using these parameters, we parameterize our radiative transfer (RT) model to simulate the total backscatter for horizontal and vertical polarizations. We then prepare a comprehensive lookup table based on the RT simulations, which is further used for training our novel deep learning-based inversion model.

Table 1. Range of parameters used in the parameterization of the two-layer regolith forward model.

Criteria	Parameter	Range
Surface roughness	Autocorrelation length [cm]	12.6
	RMS height [cm]	0–5
Physical properties	FeO+TiO$_2$ wt% [%]	0–30
	Bulk density [g/cm^3]	0.75–3.32
	Volume fraction	0–0.1
	Regolith thickness [m]	4–15
	Radius [cm]	0.5–5
Radar parameters	Incidence angle [°]	0–80
	Wavelength [cm]	12.6

2.1.2. Sensitivity Analysis of Radar Backscatter

Different lunar materials and surfaces have different dielectric constants, which affect how radar waves interact with them. Moreover, the incidence angle at which radar signals strike the surface affects the scattering properties. For example, understanding how radar backscatter changes with incidence angle can help differentiate between scattering from a rough surface and volume scattering due to buried inclusions in the regolith. To investigate the impact of incidence angle and dielectric constant on radar backscatter, we examine two scenarios with our two-layer model, as shown in Table 2. The first scenario is for sensitivity to incidence angle, while the second corresponds to the dielectric constant. For both scenarios, we consider the regolith thickness to be 5 m, the RMS height as 1 cm, and the radius of the buried rock inclusions as 1 cm with 25% volume in the regolith layer [15]. For the first scenario, we use a dielectric constant of $\varepsilon_{regolith} = 2.7 + j0.003$ for the regolith layer (corresponding to a bulk density of 1.525 g/cm^3 and 7 wt% ilmenite content) and $\varepsilon_{rock} = 8 + j0.07$ for buried rock (corresponding to solid rock with a density of 3.2 g/cm^3 and 5 wt% FeO + TiO$_2$). The incidence angle ranges between 0° and 80°. For the second scenario, a 49° incidence angle of Mini-RF is used, while the real part of the dielectric constant is varied from 2 to 10 with a fixed imaginary part of 0.003. Since we are using both east- and west-looking polar mosaics, it is necessary to examine how the incidence angle influences the radar backscatter and thus induces a bias in the prediction. Such an analysis could be important to understand the backscattering behavior of the lunar regolith before inverting the dielectric constant from Mini-RF (see Section 3.1).

Table 2. Range of parameters used in two scenarios of the forward model for sensitivity analysis.

Parameter	Scenario 1	Scenario 2
Incidence angle [°]	0–80	49
$\varepsilon_{regolith}$	2.7 + j0.003	2–10 with fixed j0.003
ε_{rock}	8 + j0.07	
Regolith thickness [m]	5	
RMS height [cm]	1	
Autocorrelation length [cm]	12.6	

Table 2. *Cont.*

Parameter	Scenario 1	Scenario 2
Radius [cm]	1	
Volume fraction	0.25	
Wavelength [cm]	12.6	

2.2. Retrieval of Dielectric Constant from Mini-RF SAR—A Deep Learning-Based Inversion Model

Deep learning algorithms are powerful tools for modeling complex systems that involve multiple variables and exhibit nonlinear behaviors [31]. When dealing with inversion problems, which possess both challenging characteristics, leveraging deep learning-based models becomes a practical choice to achieve highly accurate representations. These models are inspired by the structure and functioning of the human brain [31]. They consist of interconnected computational units called neurons. These neurons are organized into layers, with each layer responsible for specific computations. In essence, neural networks are mathematical models that can capture intricate patterns and relationships in data. The fundamental building block of a neural network is the perceptron, a simplified model of a biological neuron [31]. Perceptrons take input data, apply weights to these inputs, and then sum them up. The result is passed through an activation function to produce an output. This output is used as input for subsequent layers of the network, forming a multi-layer perceptron neural network. The architecture is inherently robust to noise [31]. The presence of multiple hidden layers in deep neural networks enhances the complex feature learning process of the network even in the presence of noise, reducing the need for rigorous data preprocessing.

Inversion problems often involve deducing the properties of a system from observed data. These problems are known for their complexity and nonlinearity, making them challenging to solve using traditional approaches. Deep learning-based models excel in handling such complexities. They can automatically discover relationships between input and output data, capturing nonlinearities and multivariate interactions that may be challenging to specify using traditional mathematical models. However, there is a caveat with deep learning: it typically requires a substantial amount of training data to generate accurate representations. This is because neural networks need numerous examples to learn and generalize from. We use the lookup table from our RT model simulations to train the deep learning model; therefore, the size of the training data is not a concern in our case. By utilizing pre-existing simulations as training data, we can leverage the advantages of deep learning without the need for massive in situ datasets.

For our setup, we fine-tuned a multi-layer perceptron neural network with five hidden layers containing 128, 64, 32, 8, and 4 nodes, respectively, to achieve a reliable and highly accurate model of inversion. The number of nodes was chosen based on a grid search. The activation function for all the layers is "ReLU", as it is known for robust performance compared to other choices in Earth-based retrieval studies [21,22] and for filtering out irrelevant variations introduced by noise [21]. As part of the input-output configurations, we have four inputs, namely incident wavelength, total radar backscatter at horizontal and vertical polarization ($\sigma^0_{total,hh}$, $\sigma^0_{total,vv}$), and incidence angle (θ), and two outputs, namely real part of dielectric constant (ε_{real}) and imaginary part of dielectric constant (ε_{imag}). Before training the model, the dataset was shuffled and then split into two parts: 20% was kept as validation data, and the remaining 80% was used for training. Moreover, during the training process, K-Fold shuffling with five folds was applied. Cross-validation with five folds aims to estimate how a model will perform and generalize on unseen, noisy data, striking a balance between two aspects, i.e., reducing both variance and bias. If we use too few folds (e.g., 2 or 3), the model's performance estimates can be highly variable, leading to unreliable assessments of its generalization capability (high variance). On the other hand, if we use too many folds (e.g., 10 or more), each fold's test set becomes very small, which can introduce bias into the performance estimates because the test data might not be

representative of the overall distribution. The inherent noise in lunar radar data is expected to be within the noise-handling capacity of multi-layer perceptrons [21,22]. Ultimately, the evaluation of the inversion model is performed by computing the statistical variables of mean squared error (*MSE*) and the coefficient of determination (R^2).

The testing of our model is performed on the Mini-RF global and polar mosaic (east and west) of horizontal and vertical components, with an incident wavelength of 12.6 cm and an incidence angle of 49°. The model output consists of dielectric constant maps, with scales set at 512 per degree for polar regions and 64 per degree for global regions (see Section 3.3). We use horizontal and vertical components because the transformation of radar polarization information into hybrid-pol Stokes parameters follows the same mathematical principles regardless of the initial scattering matrix representation [32].

2.3. Validation with Apollo Samples

To validate our inversion model, we conducted tests using 7.5 m × 15 m spatial scale Mini-RF data of the Apollo 11, 14, and 16 landing sites. Although the Mini-RF data strips cover the surroundings of Apollo 12, 15, and 17 landing sites, the exact locations of these landing sites are not covered, limiting our capability to perform validation for those sites. Since the Mini-RF resolution is coarser compared to the point-scale sample acquisition from Apollo landing sites, we considered an average of the magnitude of dielectric constant of 65 samples within the Apollo landing sites from Carrier III et al. [10]. There are a total of 12, 17, and 36 measurements from the Apollo 11, 14 and 16 landing sites, respectively. We then generated dielectric constant images for the respective sites from Mini-RF data using our inversion model. To facilitate comparison with dielectric constant measurements at the sample scale, we employed a radial averaging approach. The circle's radius started at 7.5 m, corresponding to the minimum Mini-RF spatial scale, and extended from 10 m to 40 m (encompassing an area of 5 km^2) with increments of 2 m. We ultimately visualize the variations in dielectric constant within each site, due to multiple increments, in the form of violin plots (see Section 3.2). This approach enhances confidence in comparing the inverted dielectric constant obtained from Mini-RF with laboratory-measured dielectric constants.

3. Results and Analysis

3.1. Sensitivity of Radar Backscatter to Incidence Angle and Dielectric Constant

We explore the sensitivity of radar backscatter to incidence angle while understanding the scattering processes originating from the rough surface, volume, and subsurface. This can help us identify the primary scattering at the Mini-RF incidence angle. Figure 3 shows the vertical gray area as the range of expected incidence angles for the Mini-RF data (~49°). From a statistical standpoint, it is worth noting that the backscattering coefficients for rock-subsurface interactions are identical. As a result, the yellow line labeled as "subsurface-volume" represents the combined contribution of these two scattering processes. Observing the plot, we can see that the polarized radar echo from the entire lunar regolith layer (in violet) decreases as the incidence angle increases. This decrease is observed across all five scattering terms. Surface scattering (in navy blue) dominates the polarized radar echo at small incidence angles (<25°), while scattering from buried rocks (volume scattering, in dark green) becomes the predominant process at larger incidence angles.

At the smallest incidence angles (<10°), scattering from the base of the regolith layer (in light green) becomes even more significant than volume scattering, despite the subsurface scattering contribution diminishing substantially as the incidence angle increases. The increase in the radar wave's path length within the regolith at higher incidence angles causes attenuation of the radar wave for all subsurface scattering processes. Since the subsurface volume interaction terms involve multiple scattering processes, their contribution to the overall scattering is relatively small. Therefore, it can be expected that surface and volume scattering are the two primary scattering terms to consider for S-band observations. We note that the incidence angle behaviors of the polarized radar echo strengths at S-band frequencies are consistent with Earth-based observations of the Moon [15,33].
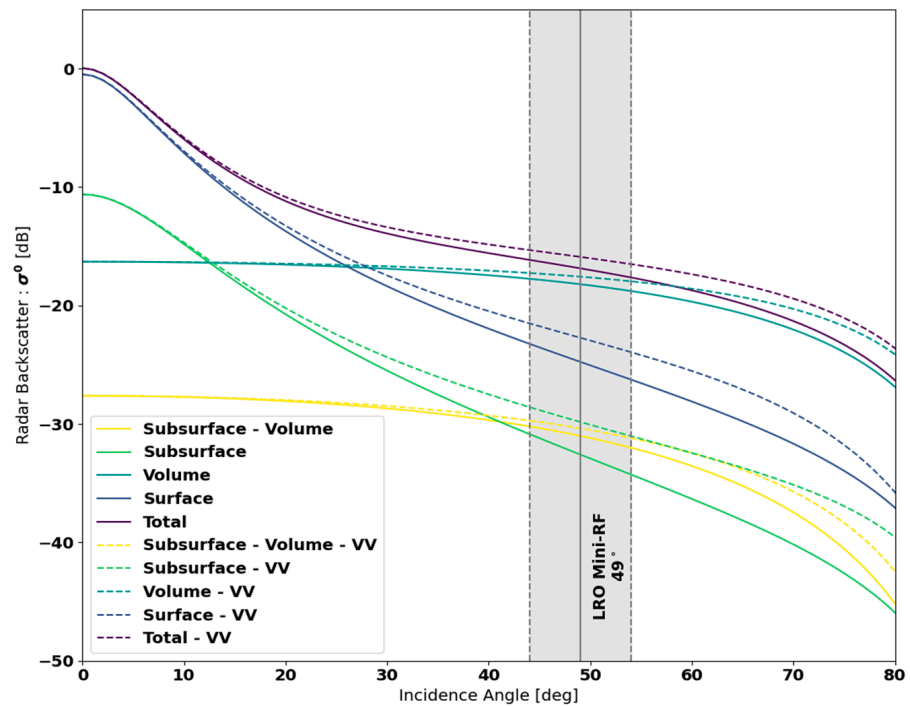
Figure 3. Sensitivity of radar backscatter to incidence angle for five scattering processes under S-band configuration.

Since our focus is to invert the dielectric constant, it is important to explore how the radar backscatter is affected by variations in dielectric constant and thereby potentially characterizing distinct lunar regolith materials. Figure 4 shows the sensitivity of radar backscatter in HH and VV polarization to the real part of the dielectric constant. As the dielectric constant increases, surface scattering also increases due to the corresponding increase in the Fresnel reflection coefficient. With higher dielectric constant values, less radar energy penetrates the subsurface, leading to a decrease in the dielectric contrast between the regolith and buried rocks.
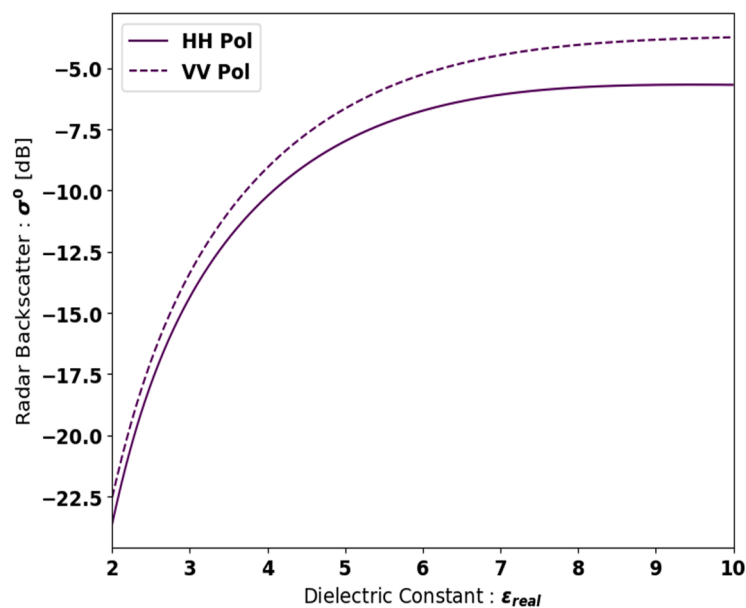

Figure 4. Sensitivity of radar backscatter to dielectric constant under S-band configuration and Mini-RF incidence angle of 49°.

The difference in magnitude between HH and VV polarizations is primarily influenced by the dominant scattering process of the regolith. We note that in the IEM, the surface is often assumed to have stronger vertical scattering components. This means that the VV polarization, which is sensitive to vertical scattering, will exhibit a higher scattering response compared to the HH polarization, which is less sensitive to vertical structures. In the lunar regolith context, we could attribute such a difference to the high population of cm- to m-scale blocky regolith layer, which contributes more towards the vertical scale (i.e., RMS height) compared to the horizontal scale (i.e., autocorrelation length).

3.2. Validation of Inversion Model with Apollo Data

The deep learning model exhibits excellent performance, with training and testing R^2 values of 0.97 and a mean squared error of 0.27 of dielectric constant. An accurate matching of R^2 values indicates that there is no overfitting in the model. Moreover, as the validation dataset remains separate from the training process, the inversion results carry greater significance and reliability, ensuring an effective fit of the model. Additionally, the average dielectric estimates from Apollo 14 and 16 samples fall within the range of average prediction, in the violin plot, made from varying radial distances, as in Figure 5. It can be observed that there are two dots in the Apollo 11 case: (a) filled, which represents the average of all 12 samples, and (b) hollow, denoting the average of 10 samples. We have used this slightly different approach for Apollo 11 to demonstrate large variability in dielectric constant within the site. Here, we found two samples (#10020 and #10057) exhibiting unusually high dielectric constants of 10.08 and 11.05 respectively, whereas the mean of the rest of the sample set is 4.92. Moreover, dielectric values greater than 10 have not been found in any of the other sites. If considered as outliers and omitted, the Apollo 11 data is consistent with the predicted dielectric constant range, as in the case of the Apollo 12 and Apollo 14 sites. For the purposes of this analysis, we have chosen to omit these data.
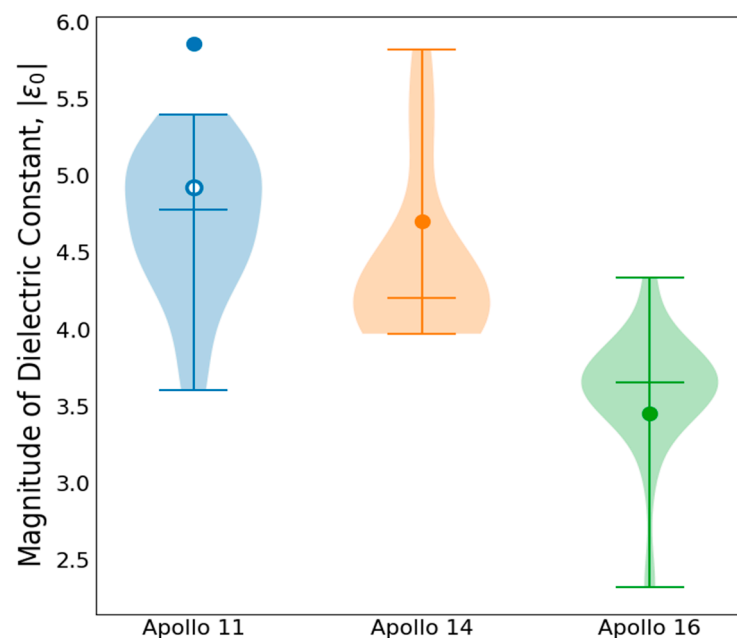

Figure 5. Comparison of predicted dielectric constant (violin plot with median lines) with ground truth (filled and hollow dots) from Apollo sites. The spread is calculated by dielectric constant radially averaged around the landing site in the radius range of 0–40 m (up to 5 km^2 area).

A justification for the omission of these data is the difference in the design of the drive core tube used while acquiring the samples in Apollo 11 compared to other Apollo missions [10]. The Apollo 11 drive core tube employed a reverse-flare bit, which was not used in any of the further Apollo missions [10]. The design of the bit posed certain

challenges during soil sampling. When the surface soil was initially loose, the shape of the bit compressed the soil upon entering the core tube, resulting in an overestimation of the in situ bulk density. Conversely, if the soil was initially dense, the shearing action of the bit loosened the soil, leading to an underestimation of the in situ density. At the same time, after sampling, it is impossible to restore the situation on the Moon: even lunar dust samples cannot be restored to their true state, which could contribute to changes in lunar morphology and density. Due to this inherent uncertainty, Scott et al. [34] could only provide a broad range for the in situ density, strongly influencing the dielectric constant. Hence, the hollow dot represents the average value, falling in the prediction range, while excluding two samples. Additionally, we include the filled dot representing the overall sample set, which shows that the model tends to underestimate the value by approximately 1.15 compared to the prediction mean at the Apollo 11 landing site.

3.3. Dielectric Constant from LRO Mini-RF

The derived maps from Mini-RF, for the first time, reveal a wide range of dielectric constant values for both the real and imaginary parts, aligning closely with laboratory-based analyses of the Apollo and Luna samples. These maps offer a valuable tool for comprehending and distinguishing the physical properties of the regolith across diverse lunar terrains at scales ranging from meters to decimeters.

3.3.1. Global Perspective

We aim to highlight the spatial variations in dielectric constant at the global scale and to understand how these dielectric changes correspond to different lunar terrains. Figure 6 reveals a notable contrast in dielectric properties between the nearside Procellarum KREEP Terrane (PKT) and the farside Feldspathic Highland Terrane (FHT). We attribute this difference to the composition of PKT mare basalt flows, which contain high levels of ilmenite ($FeO+TiO_2$). The presence of ilmenite introduces magnetic properties to the lunar regolith, and these properties greatly contribute to the absorption of radar waves. This results in a low dielectric constant in the region. However, certain localized regions within PKT, such as Kepler crater, Copernicus crater, and Aristarchus plateau, display elevated dielectric constant values. The presence of fresh Keplerian and Copernican ejecta, which contains a relatively high concentration of cm- to m-scale scatterers such as blocks at the surface, contributes to a higher bulk density of regolith. Such a distribution of ejecta materials can lead to elevated values of effective dielectric constant. This is because the electric field has more difficulty penetrating a densely packed medium. Additionally, we found dielectric anomalies associated with Aristarchus plateau, i.e., despite the low backscatter primarily due to the presence of pyroclastic deposits [35], the region shows a moderate increase in dielectric properties and differs from surrounding terrain.

The differences observed for Aristarchus are within the errors associated with the model. One potential hypothesis may be due to saturation effects of porosity on regolith. We see the potential of pyroclastic materials to preserve up to 300 ppm of indigenous water in the pores, which may saturate the pores and decrease the porosity [36,37]. The decrease could be a source of an increasing dielectric constant. However, based on dielectric constant maps alone, we cannot validate the hypothesis. This could open new research avenues for future investigation into the anomalous dielectric behavior of Aristarchus.
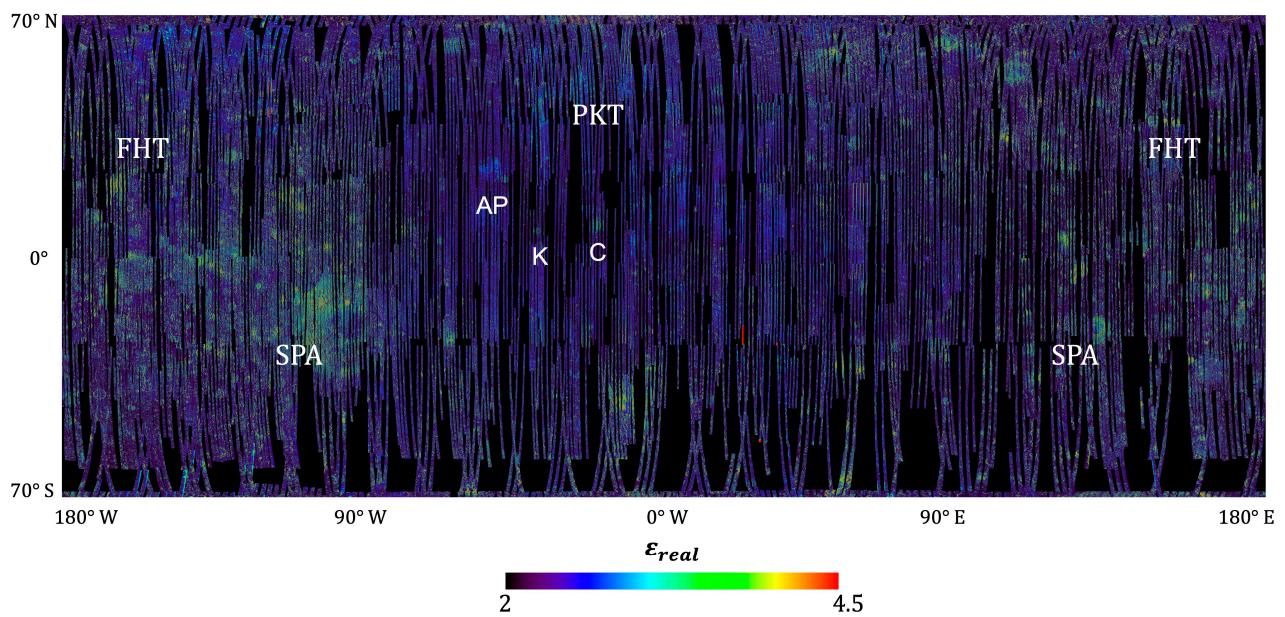
Figure 6. Real part of the dielectric constant, ε_{real}, from Mini-RF global S-band data at a spatial resolution of 64 pixels per degree. The map projection is equirectangular. AP is Aristarchus Plateau, K is Kepler crater, and C is Copernicus crater.

More importantly, the dielectric constant of Kepler and Copernicus crater ejecta surpasses that of the Aristarchus pyroclastic deposits. This discrepancy may arise because of physical and compositional variations in the regolith resulting from the impact process and the proportion of impact melt. The increased presence of rocks that may have been transported from deeper regolith layers to the surface contributes to this effect [26,35,36]. Conversely, in the case of FHTs, the blockiness of regolith observable at the radar wavelength is more pronounced compared to PKTs. As a result, radar reflections originating from the subsurface become less prominent due to increased bulk density.

The overall contrast in dielectric constant is prominently observed, likely due to the diverse composition and extensive mantling of highland materials. The distinction between FHT and PKT becomes even more evident when examining the imaginary part of the dielectric constant, where highland materials exhibit higher values compared to mare basalts (in Figure 7). One of the contributing factors to this difference is the varying proportion of ilmenite content. Specifically, the presence of ilmenite plays a more significant role than density in determining the loss tangent, which corresponds to the imaginary part of the dielectric constant. FHTs, characterized by a composition primarily composed of anorthosite or calcium-rich plagioclase feldspar, are not rich in ilmenite.

Based on our maps, it is currently challenging to differentiate the precise boundaries between the South Pole–Aitken (SPA) basin and FHT solely on dielectric properties, despite their compositional differences. However, we do observe a sub-region within the SPA basin with an elevated dielectric response. This could be attributed to the presence of a high concentration of small rocks, forming a blocky veneer on the surface, as well as unweathered ejecta deposits that impede radar penetration. Additionally, we identify distinct hotspots with high dielectric values surrounding areas of low dielectric response. This suggests the possibility of buried rocks covered by a thin superficial layer of low dielectric regolith, thereby increasing the bulk density.
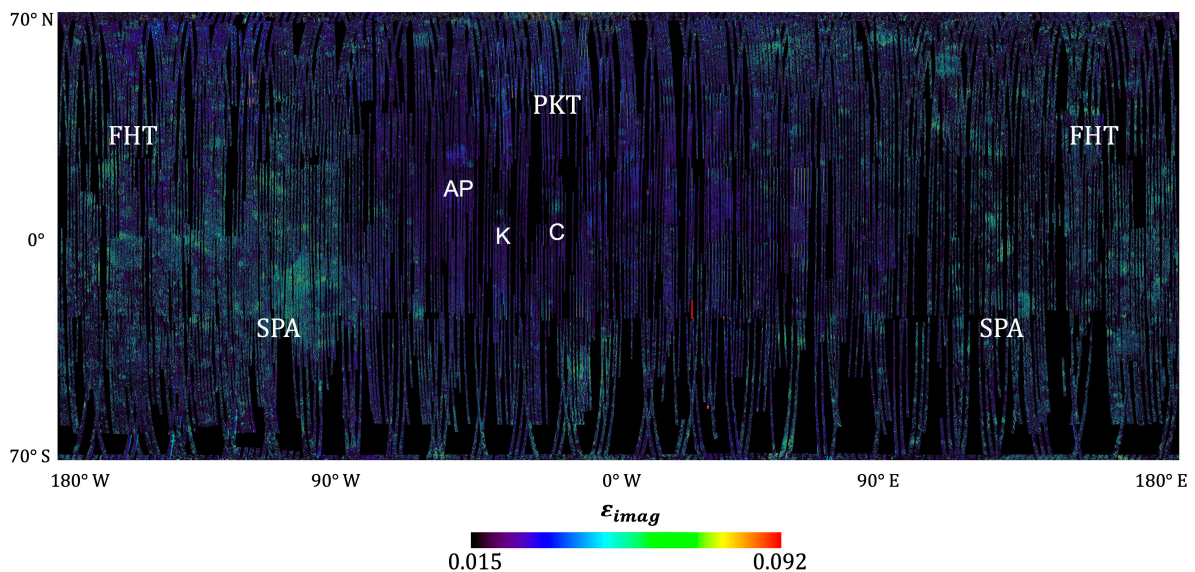
Figure 7. Imaginary part of the dielectric constant, ε_{imag}, from Mini-RF global S-band data at a spatial resolution of 64 pixels per degree. The map projection is equirectangular. AP is Aristarchus Plateau, K is Kepler crater, and C is Copernicus crater.

3.3.2. Polar Perspective

The polar regions of the Moon, both the north and south poles, are mainly characterized by highlands terrain with no clear signs of mare deposits [38]. To further investigate the physical properties of the polar terrains, we generate dielectric constant maps for a better understanding of the distinct distribution of regolith materials and the surface characterization. From Figure 8, we observe a large variation in the dielectric constant with almost similar mean values (i.e., 3.76 + j0.046 for the south pole and 3.78 + j0.047 for the north pole) and standard deviation (i.e., 0.55 + j0.018 for the south pole and 0.57 + j0.019 for the north pole).

The imaginary part shows a detailed delineation of features based on dielectric grounds better than that in the real part. Such a difference may be due to the composition of the material as the imaginary part is additionally affected by the ilmenite proportion. To estimate the bias in the prediction due to look direction, we use the east ($0°$–$180°$) and west ($180°$–$360°$) looking polar mosaics (described in Appendix A). From Figure A1, we see widespread spatial variability in the difference of dielectric constant across the polar regions. Ideally, the prediction should be the same for both look directions. However, it is interesting to note that for both the south and north poles, we see significant red-colored areas arising due to the orientation and shape of topographic features. The difference in the prediction of steeper slopes can go up to 2, but this is not the case for all the rugged and blocky regolith terrain. Higher differences are also observed in the areas (located between $70°$–$80°$N and S) that are severely hindered by stripping effects during the preparation of the mosaics. Near the poles (between $80°$–$90°$N and S), we see very minimal difference in the prediction, indicated by a mix of cyan and green color (<0.5), especially in the craters Cabeus and Rozhdestvenskiy. This could be because small-scale features and the abundance of micro-craters in the region are not significantly affected by look angle.
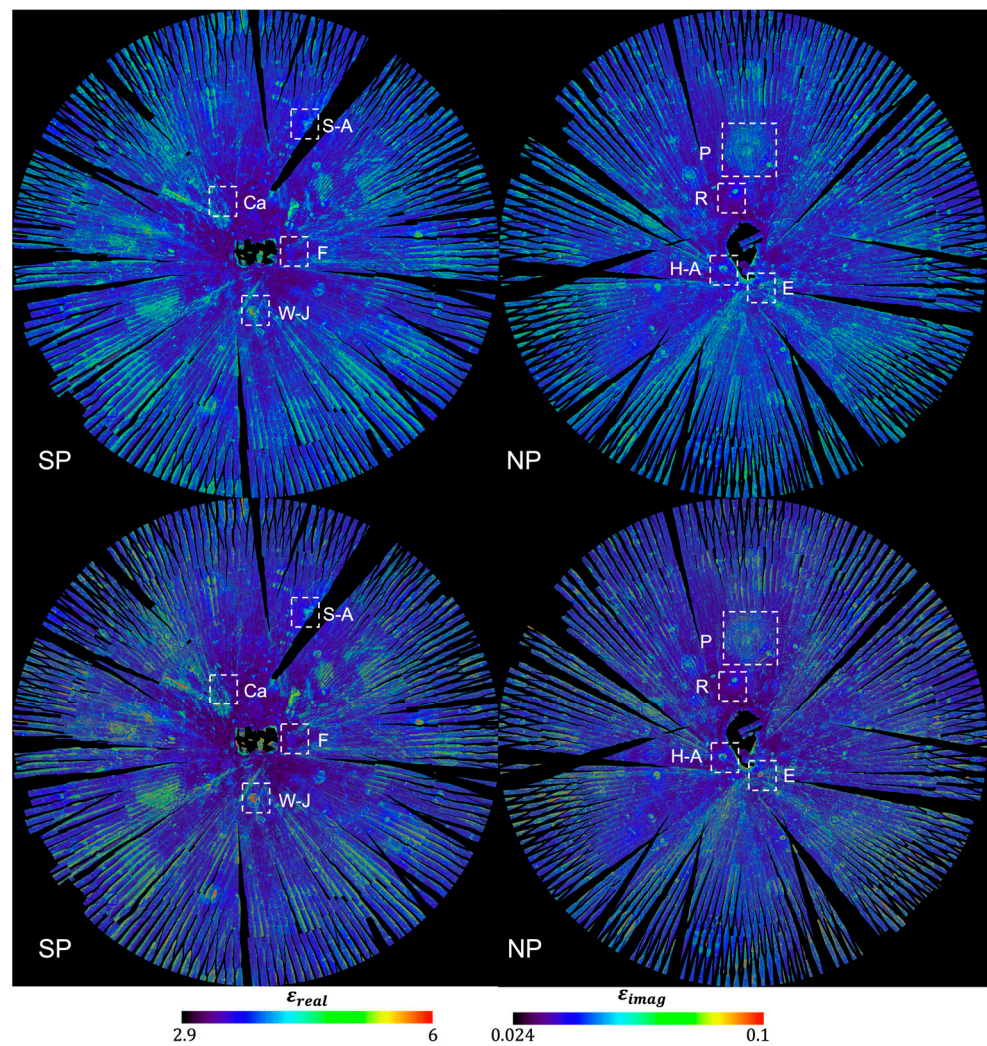
Figure 8. Estimated average real part (top) and imaginary part (bottom) of the dielectric constant from Mini-RF polar S-band data at a spatial resolution of 512 pixels per degree. Cabeus (Ca), Schomberger-A (S-A), Wiechert-J (W-J), and Faustini (F) craters are marked in the South Pole (SP), whereas Rozhdestvenskiy (R), Plaskett (P), Hermite-A (H-A), and Erlanger (E) craters are in the North Pole (NP). The map projection is polar stereographic.

From the statistical viewpoint, the mean of the difference lies close to 0 with a normal distribution for both real and imaginary parts (Figure A2), thereby commenting on the reliability and robustness of our model. We see a standard deviation of 1.1 for the real part in both the south and north poles, whereas the imaginary part has a standard deviation of 0.03. This could be used as an uncertainty in our predictions caused by look direction.

A zoomed-in version of the dielectric constant of the south polar regions is provided to demonstrate the capability of our model to differentiate the terrains at the regional scale. Figure 9a,e show the dielectric properties of Schomberger-A crater ejecta. Here, the dielectric constant is found to be spatially variable with a strong signature near the crater rim. We observe a clear dielectric boundary between rough ejecta and the surrounding terrain. In addition, a ray-like pattern can also be easily identified where the dielectric constant of the materials decreases as the distance from the crater rim increases. However, we notice that a low dielectric regolith partially blocks the high dielectric zone near the crater rim in the ejecta. This may indicate different mixing rates and composition of cm- to m-scale blocks within the deposited ejecta.
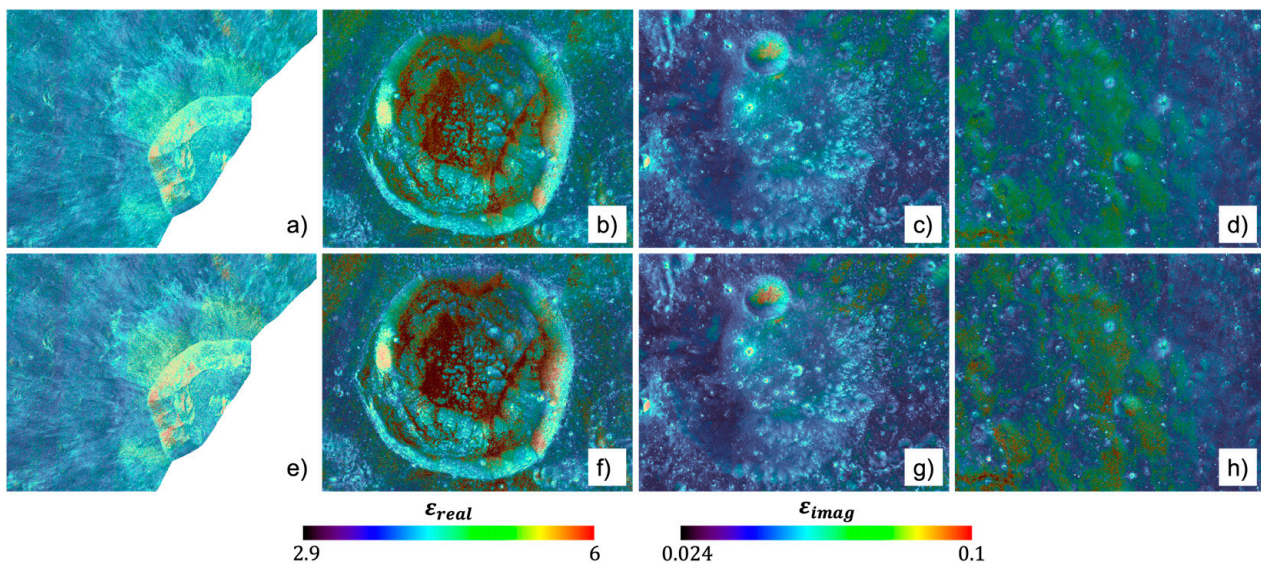
Figure 9. Real (**a**–**d**) and imaginary (**e**–**h**) parts of dielectric constant, overlain on Mini-RF S_1 image, for south polar craters Schomberger-A (**a**,**e**), Wiechert-J (**b**,**f**), Faustini (**c**,**g**), and Cabeus (**d**,**h**). The map projection is polar stereographic, and the spatial resolution is 512 pixels per degree.

On the contrary, the PSRs near south polar craters of Cabeus, Wiechert-J, and Faustini display intriguing and complex dielectric characteristics as in 89. Wiechert-J is associated with a higher dielectric constant of ~5.8 + j0.09 in the crater floor compared to the surrounding terrain outside the crater. We also notice dielectric hotspots situated in the crater walls, mainly in the northern and eastern parts, as shown in Figure 9b,f. Due to the high population of blocks in the crater floor, we expect an increased effective bulk density and hence, a dielectric constant that is higher than the intrinsic dielectric constant of the bulk regolith material. In the crater floor of Faustini, we see an elevated dielectric constant over a low dielectric regolith material (Figure 9c,g). Several patches of high dielectric constant (~5.2 + j0.08) are observed in the crater floor. This dielectric surge appears to be associated with small-scale roughness caused by secondary crater floors. In Figure 9d,h, we notice dielectric anomalous patches with larger individual spatial extent in the crater floor of Cabeus that are not associated with small crater floors as in the Faustini. Such elevated dielectric profiles in the cold traps could be attributed to either water ice exposure at the crater floor with temperatures less than 110 K or increased effective bulk density due to a significant rock population [26].

In the north polar regions, one of the most discernible features, based on dielectric properties, is the crater Plaskett (Figure 10a,e). The high population of young and fresh craters on a relatively flat crater floor displays a noticeable contrast in dielectric constant. Additionally, we observed anomalously high dielectric constant values distributed in patches in the central peak. In Figure 10b,f, we see a very strong dielectric signature ($\varepsilon_{real} > 5.5$ and $\varepsilon_{imag} > 0.8$) from the floor and some clusters on the wall of crater Hermite-A. Moreover, the surrounding terrain outside the crater exhibits a low dielectric constant, indicating the possibility of small-sized blocky materials mixed with the regolith in the crater; however, it is subjected to further analysis. Hermite-A is a younger crater compared to Erlanger and Plaskett. A similar example is demonstrated by Erlanger crater in Figure 10c,g, but with a high dielectric regolith medium outside the crater (as representative of ejecta). More importantly, we observed that the spatial extent of regions characterized by a high imaginary part of the dielectric constant differs slightly from that of the high real part. This suggests that the regolith is of absorbing nature, particularly in the Mini-RF frequency.
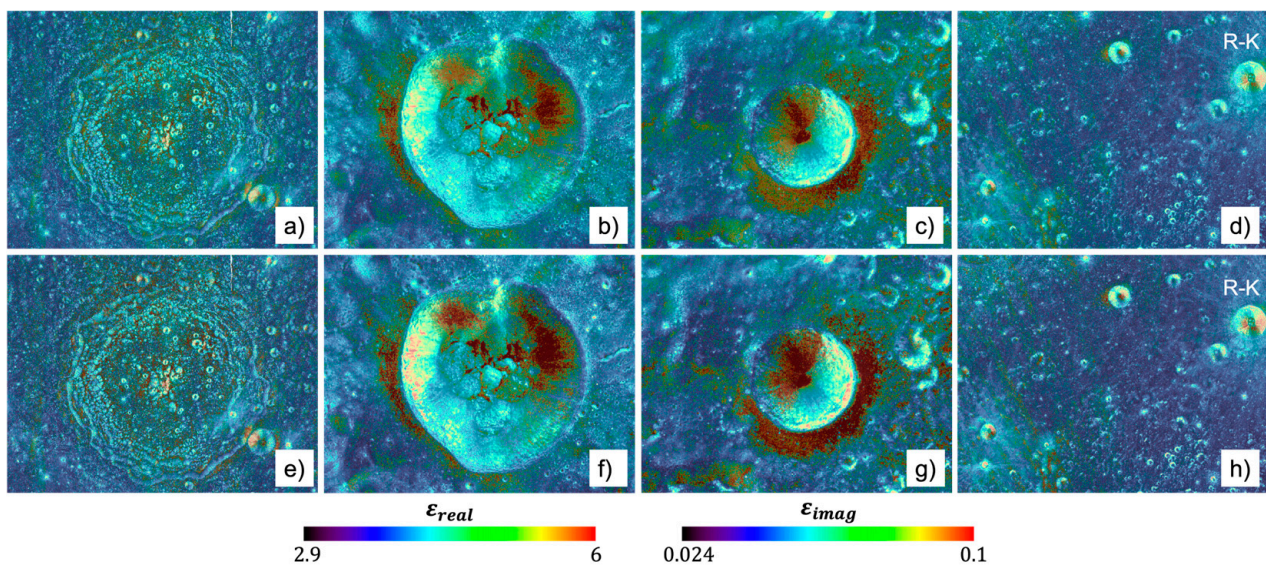
Figure 10. Real (**a–d**) and Imaginary (**e–h**) parts of the dielectric constant, overlain on Mini-RF S_1 image, for North polar craters Plaskett (**a,e**), Hermite-A (**b,f**), Erlanger (**c,g**), and Rozhdestvenskiy (**d,h**). R-K is Rozhdestvenskiy-K crater. The map projection is polar stereographic, and the spatial resolution is 512 pixels per degree.

In Figure 10d,h, we also saw a large variability in the crater floor of Rozhdestvenskiy, which is attached to the northeast rim of Plaskett. Here, an increase in dielectric constant is observed within secondary craters, with usually low dielectric constant outside the crater rims. Another prominent and relatively young crater lying on the southern rim, Rozhdestvenskiy-K, also exhibits intermediate dielectric constant values. Moreover, the low dielectric floor of Rozhdestvenskiy is found to be superficially mixed with blocky materials of intermediate dielectric constant around fresh and young secondary micro-craters distributed across the floor.

4. Discussion and Implications

Mini-RF S-band observations have been used to derive the dielectric properties of the Moon at global and polar scales. The predictions from our inversion model are in line with laboratory-measured dielectric constants of Apollo samples, proving its robustness and capability in discerning lunar materials based on dielectric grounds. The use of the east- and west-looking Mini-RF mosaics for polar regions improves dielectric prediction compared to using only one look direction. In this way, we reduce the uncertainty in our maps caused by Mini-RF's look direction. For the first time, we now understand the spatial variability of dielectric constant across the lunar surface, which could provide new insights into the vertical physical characteristics of the regolith. The observed variability in dielectric constant can mainly be attributed to differences in mineralogical content, bulk density, and the population of excavated regolith materials.

S-band radar exhibits sensitivity to scatterers at centimeter-to-meter scales. Notably distinct from typical composition of lunar regolith, certain near-surface terrains showcase unique scatterer size distributions. Among these terrains are craters and pyroclastic deposits. When focusing on young, fresh craters, radar data of the lunar surface prominently highlight their walls, floors, and ejecta blankets [39]. This is due to a substantial proportion of scatterers in the centimeter-to-meter range, which are not only deposited on the surface but also mixed within the lunar regolith (a contribution from impact melt is also possible). As a result, the dielectric constant for these craters surpasses that of the adjacent terrain due to increased effective bulk density. Moreover, the notable variations in dielectric constant within the craters could likely be caused by progressive weathering of regolith material, thereby shifting the particle size distribution towards a range that falls beyond the sensitiv-

ity of S-band radar. We thus foresee in the future to explore the relationship between the dielectric constant and crater age, similar to Bell et al. [40], Fassett et al. [41], and Nypaver et al. [42].

One potential use of our dielectric maps is in understanding the nature, abundance, and distribution of surficial water ice in the lunar PSRs. According to Heggy et al. [43], regolith fines on the floors of permanently shadowed craters smaller than 5 km in diameter are optimal targets for the unambiguous detection of water-ice enrichment using S-band radar observations. Moreover, regions with high loss tangents could indicate significant EM wave absorption at S-band frequency by the regolith, which may help determine the proportion of water-ice present in the regolith. By understanding the dielectric properties of these regions from our maps at the polar scale and their correlation with crater characteristics, we can enhance our ability to identify and study water ice in these intriguing lunar environments. The remarkably low dielectric constant and loss tangents of lunar materials, for example, in the crater floor of Rozhdestvenskiy and Cabeus or in the PKT regions, could indicate their high transparency to electromagnetic energy at S-band frequency. This means that radar waves could easily penetrate lunar soils to greater depths.

Our dielectric maps, when merged with scattering properties and other new LRO observations, could prove important in actively connecting our knowledge about the physical properties and composition of lunar surface materials. In addition, it is worth comparing the dielectric constant with the maps of H from Diviner, as both are notionally density proxies. This comparison could be made by functionally relating them and identifying whether mineralogy is the main residual. Such a combined use of measurements could refine previous interpretations of lunar terrane divisions (such as PKT, FHT, and SPA). This could further our knowledge of the evolution of physical properties and their connection with space weathering and small- or large-scale impact modification processes. At the same time, there are several telemetry methods for inverting dielectric constant from SELENE Lunar Radar Sounder (LRS) and microwave brightness temperature that could be used as an additional cross-validation source for our dielectric maps. According to Hongo et al. [44], LRS provides detailed subsurface information but requires careful interpretation of radar wave interactions. Microwave brightness temperature measurements offer broad spatial coverage but may be influenced by surface temperature and other factors. We thus emphasize the need to integrate multiple radar data sources to achieve a comprehensive understanding of the dielectric properties of the lunar surface.

5. Conclusions

Mini-RF S-band observations provide a unique opportunity to map the physical properties of lunar regolith. In this study, we present semi-controlled global and fully controlled polar S-band maps of lunar dielectric constant at 64 and 512 pixels per degree spatial resolution, respectively. These maps could be used to understand the distribution of materials within different stratigraphic layers at multiple depths. Moreover, the variability in dielectric constant can help evaluate the radar response, thereby inferring the spatial distribution of lunar features. For this, we developed a novel deep learning inversion architecture for dielectric retrievals from Mini-RF S-band data. The model is trained using data simulated from a physics-based radiative transfer model, parameterized with realistic values of physical properties from Apollo science data under Mini-RF radar configuration. We tested the trained model on S-band Mini-RF global and polar mosaics. The predictions from the model are in strong agreement with field measurements at Apollo sites. Mare basalts in the PKT exhibited low value of dielectric constant, mainly due to high ilmenite content and relatively low bulk density. We notice some localized hotspots within PKT, i.e., in the crater ejecta and pyroclastic deposits. On the contrary, there is a clear distinction in dielectric constant between PKT and highland materials of FHT. One of the reasons is the composition by itself: highland materials have low ilmenite content. It is observed that the variation in dielectric constant is influenced by changes in ilmenite content, which could easily mask the effect of density on loss tangent. Moreover, it is difficult to differentiate the

SPA and FHT using dielectric contrast. We further notice intriguing and complex dielectric properties in the PSRs of the lunar south and north poles, providing an opportunity to quantify the fractional volume of water ice content in the polar regolith. In this regard, our findings highlight the capability of the inversion model to capture subtle differences in dielectric constant due to surface composition and buried volumes discernible at Mini-RF radar wavelengths. From the sensitivity study, we found that for S-band, radar backscatter decreases with incidence angle but increases with dielectric constant at Mini-RF incidence angles. Our dielectric constant maps can thus be utilized to understand the lunar surface processes at global and polar scales, which could play an important role in ARTEMIS mission planning.

Currently, the inversion model is also capable of producing dielectric maps of polar regions at the highest available spatial resolution of 2048 pixels per degree. The future scope of our study is to calibrate the model for local incidence angles. We expect the model to perform better in capturing the finest details of the regolith, when provided with local incidence angle information. We also aim to use advanced radiative transfer theories for better representation of lunar regolith. For instance, the use of the dense radiative transfer model (DMRT) [45] could be an optimal option for quantifying radar backscatter as a function of physical properties. Moreover, the advanced integral equation model (AIEM) [46] is valid over large scales of roughness and performs better in simulating rough surface scattering processes than traditional physics-based models, such as IEM. This could provide an opportunity to include a wide range of realistic roughness values while training the model. We also intend to improve our deep learning model in terms of input-output configuration, i.e., to invert both surface roughness and dielectric constant. Such an output could help us separate the contribution of roughness from volume scattering processes, thereby quantifying the water ice content from SAR observations.

We note that there might be moisture contamination in Apollo samples [4–7], which could lead to unreliable dielectric constant measurements. However, in Strangway and Olhoeft [7], the effect of moisture levels on the dielectric constant is found to be most significant at lower frequencies, i.e., <10 kHz, wherein the loss tangent increases drastically by almost a factor of 20. We thus recommend analyzing more returned lunar samples from future lunar missions with great care, ensuring negligible effect of moisture on the results. This will also greatly help the planetary remote sensing community validate inversion frameworks with great confidence. As an alternative, lunar meteorites and sample-returned rocks could also be used as proxies for lunar regolith (particularly regolith breccias or Apollo/Luna regolith powders). In fact, new techniques could be useful for studying the porosity and mechanical properties of meteorites, which might be used as simulants for future laboratory studies (e.g., [47,48]). In addition, using a tomographic technique, we could identify the main minerals, density, and moisture levels in each sample (even on the subsurface) that impact the dielectric constant and thus could be useful in testing our model. At the same time, conducting experiments under varying conditions and with different techniques can present a challenge for direct comparison. Given that we know the relationship between dielectric constant, density, moisture levels, and temperature, there exist normalization methods that could provide a unified measurement value [4–7]. Once the data is normalized, statistical methods such as regression analysis or multivariate analysis can be employed to compare the results across different conditions. These techniques are standard in the field and provide a robust framework for analyzing and comparing the dielectric properties of lunar samples. Furthermore, to mitigate this, we foresee the combined use of dielectric constant maps augmented with other LRO, Chandrayaan-2 products, and compositional information to infer the evolution of lunar features due to weathering and impact cratering processes.

Appendix A

To understand the variations in the prediction of dielectric constant due to the look direction, we calculate the difference in dielectric constant between the east and west look directions. The difference maps are shown in Figure A1, with their respective frequency distributions in Figure A2.
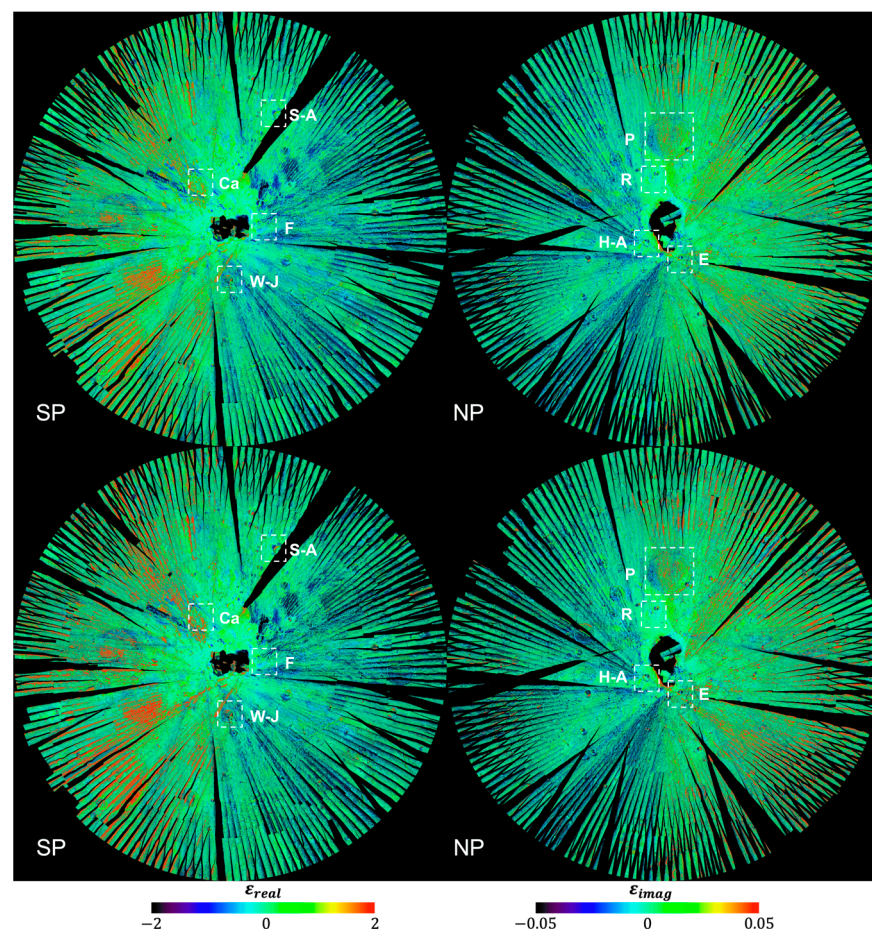

Figure A1. Difference maps of the real part (top) and imaginary part (bottom) of the dielectric constant from Mini-RF polar S-band data at a spatial resolution of 512 pixels per degree. Cabeus

(Ca), Schomberger-A (S-A), Wiechert-J (W-J), and Faustini (F) craters are marked in the South Pole (SP), whereas Rozhdestvenskiy (R), Plaskett (P), Hermite-A (H-A), and Erlanger (E) craters are in the North Pole (NP). The map projection is polar stereographic.
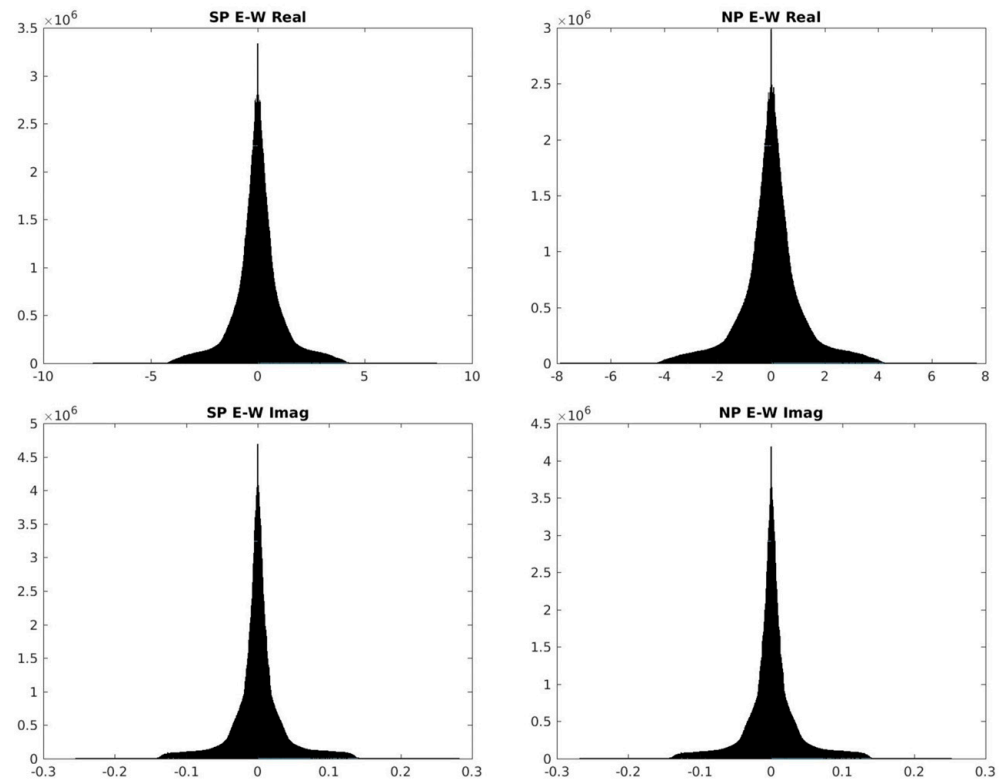

Figure A2. Histogram of difference maps of the real (top) and imaginary (bottom) parts of the dielectric constant for the south pole (left) and north pole (right).

References

1. Jolliff, B.L.; Gillis, J.J.; Haskin, L.A.; Korotev, R.L.; Wieczorek, M.A. Major lunar crustal terranes: Surface expressions and crust-mantle origins. *J. Geophys. Res. Planets* **2000**, *105*, 4197–4216. [CrossRef]
2. Cahill, J.T.; Thomson, B.J.; Patterson, G.W.; Bussey DB, J.; Neish, C.D.; Lopez, N.R.; Pasckert, J.H. The Miniature Radio Frequency instrument's (Mini-RF) global observations of Earth's Moon. *Icarus* **2014**, *243*, 173–190. [CrossRef]
3. Wieczorek, M.A.; Phillips, R.J. The "Procellarum KREEP Terrane": Implications for mare volcanism and lunar evolution. *J. Geophys. Res. Planets* **2000**, *105*, 20417–20430. [CrossRef]
4. Olhoeft, G.R.; Strangway, D.W. Electrical properties of the surface layers of Mars. *Geophys. Res. Lett.* **1974**, *1*, 141–143. [CrossRef]
5. Olhoeft, G.R.; Frisillo, A.L.; Strangway, D.W. Electrical Properties of Lunar Soil Sample 15301,38. *J. Geophys. Res.* **1974**, *79*, 1599–1604. [CrossRef]
6. Olhoeft, G.R.; Strangway, D.W. Dielectric properties of the first 100 m of the Moon. *Earth. Planet. Sci. Lett.* **1975**, *24*, 394–404. [CrossRef]
7. Strangway, D.W.; Olhoeft, G.R. Electrical Properties of Planetary Surfaces. *Philos. Trans. R. Soc. Lond. Ser. A Math. Phys. Sci.* **1977**, *285*, 441–450.
8. Qian, Y.; Xiao, L.; Wang, Q.; Head, J.W.; Yang, R.; Kang, Y.; van der Bogert, C.H.; Hiesinger, H.; Lai, X.; Wang, G.; et al. China's Chang'E-5 landing site: Geology, stratigraphy, and provenance of materials. *Earth Planet. Sci. Lett.* **2021**, *561*, 116855. [CrossRef]
9. Li, C.; Hu, H.; Yang, M.-F.; Pei, Z.-Y.; Zhou, Q.; Ren, X.; Liu, B.; Liu, D.; Zeng, X.; Zhang, G.; et al. Characteristics of the lunar samples returned by the Chang'E-5 mission. *Natl. Sci. Rev.* **2022**, *9*, nwab188. [CrossRef]
10. Carrier, W.D., III; Olhoeft, G.R.; Mendell, W. Physical Properties of the Lunar Surface. In *Lunar Sourcebook*; Cambridge University Press: Cambridge, MA, USA, 1991; pp. 475–594.
11. Ghent, R.R.; Leverington, D.W.; Campbell, B.A.; Hawke, B.R.; Campbell, D.B. Earth-based observations of radar-dark crater haloes on the Moon: Implications for regolith properties. *J. Geophys. Res. Planets* **2005**, *110*, E02005. [CrossRef]
12. Campbell, B.A.; Campbell, D.B.; Margot, J.L.; Ghent, R.R.; Nolan, M.; Chandler, J.; Carter, L.M.; Stacey, N.J.S. Focused 70-cm wavelength radar mapping of the Moon. *IEEE Trans. Geosci. Remote Sens.* **2007**, *45*, 4032–4042. [CrossRef]
13. Chin, G.; Brylow, S.; Foote, M.; Garvin, J.; Kasper, J.; Keller, J.; Litvak, M.; Mitrofanov, I.; Paige, D.; Raney, K.; et al. Lunar reconnaissance orbiter overview: The instrument suite and mission. *Space Sci. Rev.* **2007**, *129*, 391–419. [CrossRef]

14. Nozette, S.; Spudis, P.; Bussey, B.; Jensen, R.; Raney, K.; Winters, H.; Lichtenberg, C.L.; Marinelli, W.; Crusan, J.; Gates, M.; et al. The Lunar Reconnaissance Orbiter Miniature Radio Frequency (Mini-RF) Technology Demonstration. *SSR* **2010**, *150*, 285–302.

15. Fa, W.; Wieczorek, M.A.; Heggy, E. Modeling polarimetric radar scattering from the lunar surface: Study on the effect of physical properties of the regolith layer. *J. Geophys. Res.* **2011**, *116*, E03005. [CrossRef]

16. Campbell, B.A.; Arvidson, R.E.; Shepard, M.K. Radar polarization properties of volcanic and playa surfaces: Applications to terrestrial remote sensing and Venus data interpretation. *J. Geophys. Res. Planets* **1993**, *98*, 17099–17113. [CrossRef]

17. Campbell, B.A.; Grant, J.; Maxwell, T. Radar penetration in Mars analog environments. In Proceedings of the 33rd Lunar and Planetary Science Conference, Houston, TX, USA, 11–15 March 2002; p. 1616.

18. Liu, N.; Ye, H.; Jin, Y.-Q. Dielectric inversion of lunar PSR media with topographic mapping and comment on "quantification of water ice in the Hermite-A crater of the lunar north pole. *IEEE Geosci. Remote Sens. Lett.* **2017**, *14*, 1444–1448. [CrossRef]

19. Kumar, A.; Kochar, I.M.; Pandey, D.K.; Das, A.; Putrevu, D.; Kumar, R.; Panigrahi, R.K. Dielectric Constant Estimation of Lunar Surface Using Mini-RF and Chandrayaan-2 SAR Data. *IEEE Trans. Geosci. Remote Sens.* **2022**, *60*, 4600608. [CrossRef]

20. Cloude, S.R.; Goodenough, D.G.; Chen, H. Compact decomposition theory. *IEEE Geosci. Remote Sens. Lett.* **2012**, *9*, 28–32. [CrossRef]

21. Baghdadi, N.; Gaultier, S.; King, C. Retrieving surface roughness and soil moisture from synthetic aperture radar (SAR) data using neural networks. *Can. J. Remote Sens.* **2002**, *28*, 701–711. [CrossRef]

22. Shukla, S. Lunar Regolith Characterization for Solar Wind Implanted Helium-3 Using M^3 Spectroscopy and Bistatic Miniature Radar. Master's Thesis, University of Twente Faculty of Geo-Information Science and Earth Observation (ITC), Enschede, The Netherlands, 2019.

23. Shukla, S.; Tolpekin, V.; Kumar, S.; Stein, A. Investigating the Retention of Solar Wind Implanted Helium-3 on the Moon from the Analysis of Multi-Wavelength Remote Sensing Data. *Remote Sens.* **2020**, *12*, 3350. [CrossRef]

24. Sharma, A.; Kumar, S.; Bhiravarasu, S.S. Integral equation modeling for dielectric retrieval of the lunar surface using Chandrayaan-2 fully-Polarimetric L-band dual frequency SAR (DFSAR) data. *Icarus* **2023**, *391*, 115350. [CrossRef]

25. Gao, Y.; Dang, Y.; Lu, P.; Hou, W.; Zhao, F.; Wang, B.; Yu, W.; Wang, R. Investigating the dielectric properties of lunar surface regolith fines using Mini-RF SAR data. *ISPRS J. Photogramm. Remote Sens.* **2023**, *197*, 56–70. [CrossRef]

26. Patterson, G.; Stickle, A.; Turner, F.; Jensen, J.; Bussey, D.; Spudis, P.; Espiritu, R.; Schulze, R.; Yocky, D.; Wahl, D.; et al. Bistatic radar observations of the Moon using Mini-RF on LRO and the Arecibo Observatory. *Icarus* **2017**, *283*, 2–19. [CrossRef]

27. Raney, K. Dual polarized SAR and Stokes parameters. *Geosci. Remote Sens. Lett.* **2006**, *3*, 317–319. [CrossRef]

28. Kirk, R.L.; Becker, T.L.; Shinaman, J.; Edmundson, K.L.; Cook, D.; Bussey, D.B.J. A Radargrammetric Control Network and Controlled Mini-RF Mosaics of the Moon's North Pole . . . at Last! In Proceedings of the 44th Annual Lunar and Planetary Science Conference, Ser. Lunar and Planetary Science Conference, The Woodlands, TX, USA, 18–22 March 2013; p. 2920.

29. Fung, A.K.; Chen, K.S. *Microwave Scattering and Emission Models for Users*; Artech House Publishers: Norwood, MA, USA, 2010; ISBN 1608070379.

30. Fung, A.K.; Li, Z.; Chen, K.S. Backscattering from a Randomly Rough Dielectric Surface. *IEEE Trans. Geosci. Remote Sens.* **1982**, *30*, 356–369. [CrossRef]

31. Atkinson, P.M.; Tatnall, A.R.L. Introduction Neural networks in remote sensing. *Int. J. Remote Sens.* **2010**, *18*, 699–709. [CrossRef]

32. Raney, R.K.; Cahill, J.T.S.; Patterson, G.W.; Bussey, D.B.J. The m-chi decomposition of hybrid dual-polarimetric radar data with application to lunar craters. *J. Geophys. Res. Planets* **2012**, *117*, 1–8. [CrossRef]

33. Thompson, T.W. High-resolution lunar radar map at 70-cm wavelength. *Earth Moon Planets* **1987**, *37*, 59–70. [CrossRef]

34. Scott, R.F.; Carrier, W.D., III; Costes, N.C.; Mitchell, J.K. Apollo 12 soil mechanics investigation. *Geotechnique* **1971**, *21*, 1–14. [CrossRef]

35. Morgan, G.A.; Jawin, E.R.; Campbell, B.A.; Patterson, G.W.; Bramson, A.M.; Nypaver, C.A.; Stopar, J.D.; Jozwiak, L.M.; Stickle, A.M.; Bhiravarasu, S.S. Radar Perspective of the Aristarchus Pyroclastic Deposit and Implications for Future Missions. *Planet. Sci. J.* **2023**, *4*, 209. [CrossRef]

36. Campbell, B.A.; Carter, L.M.; Hawke, B.R.; Campbell, D.B.; Ghent, R.R. Volcanic and impact deposits of the Moon's Aristarchus Plateau: A new view from Earth-based radar images. *Geology* **2008**, *36*, 135–138. [CrossRef]

37. Chevrel, S.D.; Pinet, P.C.; Daydou, Y.; Le Mouélic, S.; Langevin, Y.; Costard, F.; Erard, S. The Aristarchus Plateau on the Moon: Mineralogical and structural study from integrated Clementine UV-Vis-NIR spectral data. *Icarus* **2009**, *199*, 9–24. [CrossRef]

38. Spudis, P.D.; Bussey, D.B.J.; Baloga, S.M.; Cahill, J.T.S.; Glaze, L.S.; Neish, C.D.; Patterson, G.W.; Raney, R.K.; Thompson, T.W.; Thomson, B.J.; et al. Evidence for water ice on the Moon: Results for anomalous polar craters from the LRO Mini-RF imaging radar. *J. Geophys. Res. Planets* **2013**, *118*, 2016–2029. [CrossRef]

39. Neish, C.D.; Bussey, D.B.J.; Spudis, P.; Marshall, W.; Thomson, B.J.; Patterson, G.W.; Carter, L.M. The nature of lunar volatiles as revealed by Mini-RF observations of the LCROSS impact site. *J. Geophys. Res.* **2011**, *116*, E01005. [CrossRef]

40. Bell, S.W.; Thomson, B.J.; Dyar, M.D.; Neish, C.D.; Cahill, J.T.S.; Bussey, D.B.J. Dating small fresh lunar craters with Mini-RF radar observations of ejecta blankets. *J. Geophys. Res.* **2012**, *117*, E00H30. [CrossRef]

41. Fassett, C.I.; King, I.R.; Nypaver, C.A.; Thomson, B.J. Temporal evolution of S-band circular polarization ratios of kilometer-scale craters on the lunar maria. *J. Geophys. Res. Planets* **2018**, *123*, 3133–3143. [CrossRef]

42. Nypaver, C.A.; Thomson, B.J.; Fassett, C.I.; Rivera-Valentín, E.G.; Patterson, G.W. Prolonged rock exhumation at the rims of kilometer-scale lunar craters. *J. Geophys. Res. Planets* **2021**, *126*, e2021JE006897. [CrossRef]

43. Heggy, E.; Palmer, E.; Thompson, T.; Thomson, B.; Patterson, G. Bulk composition of regolith fines on lunar crater floors: Initial investigation by LRO/Mini-RF. *Earth Planet. Sci. Lett.* **2020**, *541*, 116274. [CrossRef]

44. Hongo, K.; Toh, H.; Kumamoto, A. Correction to: Estimation of bulk permittivity of the Moon's surface using Lunar Radar Sounder on-board Selenological and Engineering Explorer. *Earth Planets Space* **2021**, *73*, 55. [CrossRef]

45. Wen, B.; Tsang, L.; Winebrenner, D.; Ishimaru, A. Dense medium radiative transfer theory: Comparison with experiment and application to microwave remote sensing and polarimetry. *IEEE Trans. Geosci. Remote Sens.* **1990**, *28*, 46–59. [CrossRef]

46. Wu, T.-D.; Chen, K.-S.; Shi, J.C.; Lee, H.-W.; Fung, A.K. A Study of an AIEM Model for Bistatic Scattering From Randomly Rough Surfaces. *IEEE Trans. Geosci. Remote Sens.* **2008**, *46*, 2584–2598.

47. Kiefer, W.S.; Macke, R.J.; Britt, D.T.; Irving, A.J.; Consolmagno, G.J. The density and porosity of lunar rocks. *Geophys. Res. Lett.* **2012**, *39*, L07201. [CrossRef]

48. Peña-Asensio, E.; Trigo-Rodríguez, J.M.; Sort, J.; Ibáñez-Insa, J.; Rimola, A. Mechanical properties of minerals in lunar and HED meteorites from nanoindentation testing: Implications for space mining. *Meteorit. Planet Sci.* **2024**, *59*, 1297–1313. [CrossRef]